Loss-of-function mutations in *MICU1* cause a brain and muscle disorder linked to primary alterations in mitochondrial Ca^{2+} signalling.

Clare V Logan[1^], György Szabadkai[2,3^], Jenny A Sharpe[2^], David A Parry[1], Silvia Torelli[4], Anne-Marie Childs[5], Marjolein Kriek[6], Rahul Phadke[4,7], Colin A Johnson[1], Nicola Y Roberts[1], David T Bonthron[1], Karen A Pysden[5], Tamieka Whyte[4], Iulia Munteanu[4], A Reghan Foley[4], Gabrielle Wheway[1], Katarzyna Szymanska[1], Subaashini Natarajan[1], Zakia A Abdelhamed [1], Joanne E Morgan[1], Helen Roper[8], Gijs WE Santen[6], Erik H Niks[9], W Ludo van der Pol[10], Dick Lindhout[11], Anna Raffaello[3], Diego De Stefani[3], Johan T den Dunnen[6] , Yu Sun[6], Ieke Ginjaar[6], Caroline A Sewry[4], Matthew Hurles[12], Rosario Rizzuto[3], UK10K[13], Michael R Duchen[2^*], Francesco Muntoni[4^*], Eamonn Sheridan[1^*]

Author affiliation

[1] Leeds Institute of Biomedical and Clinical Science, Wellcome Trust Brenner Building, St James's University Hospital, Leeds LS9 7TF, UK

[2]University College London, Department of Cell and Developmental Biology, Consortium for Mitochondrial Research, London, UK

[3]Department of Biomedical Sciences, University of Padua and CNR Neuroscience Institute, Padua, Italy

[4]UCL Institute of Child Health, Dubowitz Neuromuscular Centre and MRC Centre for Neuromuscular Diseases, London, UK

[5]Department of Paediatric Neurology, Leeds General Infirmary, Leeds, UK

[6]Center for Human and Clinical Genetics, Department of Clinical Genetics, Leiden University Medical Center, Leiden, the Netherlands

[7]UCL Institute of Neurology, MRC Centre for Neuromuscular Diseases, London, UK

[8]Department of Paediatrics, Birmingham Heartlands Hospital, Birmingham, UK

[9]Department of Neurology, Leiden University Medical Center, Leiden, the Netherlands

[10]Department of Neurology & Neurosurgery, Brain Center Rudolf Magnus, University Medical Center Utrecht, Utrecht, the Netherlands.

[11]Department of Clinical Genetics, University Medical Center Utrecht, Utrecht, the Netherlands

[12]Wellcome Trust Sanger Institute, Cambridge, UK

[13] UK10K Consortium (see Supplementary Note)

^Equally contributing

*Corresponding author

Correspondence should be addressed to:

E.Sheridan@leeds.ac.uk

m.duchen@ucl.ac.uk

f.muntoni@ucl.ac.uk

Abstract

Mitochondrial Ca^{2+} uptake plays key roles in cell life and death. Physiological Ca^{2+} signalling regulates aerobic metabolism, while pathological Ca^{2+} overload triggers cell death. The process is mediated by the Ca^{2+} uniporter complex in the inner mitochondrial membrane, which includes MCU[1], a Ca^{2+}-selective ion channel and its regulator, MICU1[2]. Here we report mutations of *MICU1* in patients with a novel disease phenotype characterised by proximal myopathy, learning difficulties and a progressive extrapyramidal movement disorder. In fibroblasts from patients with *MICU1* mutations, agonist-induced mitochondrial Ca^{2+} uptake at low cytosolic $[Ca^{2+}]$ was increased and cytosolic Ca^{2+} signals were reduced. Whilst resting mitochondrial membrane potential was unchanged in MICU1-deficient cells, the mitochondrial network was severely fragmented. While the pathophysiology of muscular dystrophy[3] and the core myopathies[4] involves abnormal mitochondrial Ca^{2+} handling, the *MICU1* deficiency phenotype is caused by a primary defect in mitochondrial Ca^{2+} signaling, demonstrating the crucial role of mitochondrial Ca^{2+} uptake in man.

Main text

Mitochondrial Ca^{2+} homeostasis plays key roles in many aspects of cell physiology[5]. Cellular Ca^{2+} signals that mediate secretion, contraction or excitability are invariably coupled with mitochondrial Ca^{2+} uptake, which in turn modulates mitochondrial bioenergetic function[5-7], buffers cytosolic Ca^{2+} signals[6,8], and regulates Ca^{2+}-mediated pathways leading to programmed and necrotic cell death[9]. The mitochondrial membrane potential ($\Delta\Psi_m$) drives Ca^{2+} transport through the mitochondrial Ca^{2+} uniporter (MCU)[1]. MCU is regulated by mitochondrial calcium uptake 1 (MICU1), which confers Ca^{2+} sensitivity to the pathway[2,10]. The physiological roles of the proteins involved in regulating mitochondrial calcium transport are only partially understood[11-13], and mostly derive from silencing experiments in cell culture systems, sometimes with conflicting results.

We studied a cohort of patients who presented in childhood with a distinctive clinical phenotype, comprising early onset proximal muscle weakness with a static course and moderately to grossly elevated serum creatine kinase (CK), accompanied by learning difficulties (Supplementary Table 1). Subsequently, subtle extrapyramidal motor signs appeared in 10/15 patients; this progressed over the course of several years to a debilitating disorder of involuntary movement, with variable features including chorea, tremor, dystonic posturing, and oro-facial dyskinesia. Additional variable features included ataxia, microcephaly, ophthalmoplegia, ptosis, optic atrophy and an axonal peripheral neuropathy, all of which suggest a possible mitochondrial disorder. However, no patients had diabetes mellitus, deafness or cardiomyopathy, and respiratory chain enzyme analysis was normal in muscle biopsies of all cases tested (Supplementary Table 2). In patient 4 cerebral MRI showed abnormal high signal in the globus pallidus, suggestive of mitochondrial disease. (Supplementary Fig. 1)

Muscle biopsies were available in 6/15 cases. All showed myopathic features with diffuse variation in fibre size, increased internal and central nuclei (Fig.1a) and clusters of regenerating fibres (Fig.1b), without pronounced fibrosis or fatty infiltration. Necrotic fibres

were rare except in one case (8b). Fibre typing was preserved and frequent focal areas devoid of mitochondria (mini-cores) were observed in both fibre types in the 5 biopsies taken above 6 years of age (Fig.1c,d).

The consanguineous structure of Family 1 suggested autosomal recessive inheritance (Fig. 2a). We therefore performed homozygosity analysis using the Affymetrix Genome-Wide Human SNP Array 6.0. Genotype data were analyzed using SnpViewer (see URLs) and IBDfinder software[14]. A single region of concordant homozygosity, shared by the affected individuals, was identified on chromosome 10 at position 73,825,652-78,713,115 (Fig. 2b).

Whole exome sequencing of case 2a (Fig. 1a) revealed only one potentially pathogenic variant within the homozygous region; a splice acceptor site mutation c.1078-1G>C in *MICU1* NM_006077.3(Fig. 2c). This variant segregated with the phenotype in Family 1, and was not seen in 22 ethnically matched in-house exomes, nor in 372 ethnically matched control alleles analysed by PCR. Whole exome sequencing of two further affected individuals (UK10K_NM5061923 and UK10K_NM5061924, cases 8a and 8b respectively) was performed concurrently, as part of the UK10K project, with variants called and filtered as previously described[15]. The homozygous c.1078-1G>C variant was again found in both of these patients. This variant is absent from dbSNP 137, the 1000 Genomes database, the NHLBI exome variant server of 6500 exomes, the UK10K twins cohort and the ClinSeq study. Sanger sequencing (Supplementary Table 3) identified the same variant in a further 6 affected individuals from 3 UK Pakistani families. In contrast, whole exome sequencing of two unrelated Dutch Caucasian families (cases LUMC1 & 2, UMCU1 & 2; Supplementary Fig.2,3), in which children presented with a proximal myopathy, elevated CK, and a movement disorder revealed a different homozygous mutation, affecting a splice donor site, c.741+1G>A (Fig. 2c). A total of 15 patients, from 7 families were identified. Neither the UK Pakistani families, nor the Caucasian Dutch families were knowingly related to each other, however genotype data from microsatellites flanking *MICU1* suggest a common ancestral origin for individuals carrying each of the two variants (Supplementary Fig. 4). All variant and phenotype data were submitted to the *MICU1* gene variant database (see URLs).

Sequencing of cDNA (Supplementary Table 4) from patients with each of the splice site mutations showed intronic insertions causing frameshifts (Supplementary Fig. 5,6). The patient transcripts were shown by qPCR to undergo nonsense-mediated decay (Fig. 2d), and loss of protein was confirmed by western blot (Supplementary Fig. 7). Consistent with the clinical features displayed by patients, *Micu1* was highly expressed in normal mouse muscle and brain (Supplementary Fig. 8,9).

To evaluate the physiological consequences of the absence of MICU1, we analysed cellular and mitochondrial Ca^{2+} homeostasis in primary fibroblasts from two healthy individuals and two unrelated patients (cases 6 and 8a, see Supplementary Table 1, Supplementary Fig. 10,11) in resting cells and following stimulation with a Ca^{2+}-mobilising agonist (histamine, 10 μM). Mitochondrial ($[Ca^{2+}]_m$) and cytosolic ($[Ca^{2+}]_c$) Ca^{2+} concentration was measured using mitochondrially targeted aequorin[1] and fluo-4, respectively. The initial rate of histamine-induced mitochondrial Ca^{2+} uptake was increased in MICU1-deficient fibroblasts (Fig 3a,b), indicating increased mitochondrial Ca^{2+} load at lower $[Ca^{2+}]_c$, while the peak $[Ca^{2+}]_m$ was unchanged (Fig 3c). The increased velocity of Ca^{2+} uptake was not due to differences in mitochondrial membrane potential ($\Delta\Psi_m$) (Fig. 3d) or altered endoplasmic reticulum (ER) Ca^{2+} content (Supplementary Fig. 12a). An increased rate of mitochondrial calcium uptake

could result from an increased proximity of the mitochondrial pool to the ER, thus exposing the mitochondria to higher microdomains of calcium. We have therefore explored this proximity using immunofluorescence. The data do not reveal any significant change in ER mitochondrial proximity (Supplementary Fig.13). While we recognize that EM data might be more precise, it is important to note that changes in ER/mitochondrial contacts due to altered expression of related proteins can be observed in this way[16,17].

Since aequorin is not suitable for the quantification of low submicromolar $[Ca^{2+}]$[18], in order to better appreciate the relationship between cytosolic and mitochondrial $[Ca^{2+}]$ close to basal levels, we used rhod-2 loaded cells for high temporal resolution imaging, which probe has higher Ca2+ affinity and also allows the simultaneous measurement of $[Ca^{2+}]$ in both compartments[19]. Despite the limitations inherent in this assay, resting $[Ca^{2+}]_m$ was significantly higher, and the velocity of mitochondrial Ca^{2+} uptake was significantly increased in the patient derived MICU1-deficient cells (Fig 3e-j). The elevated $[Ca^{2+}]_m$ at rest was confirmed by ratiometric measurements using the recombinant 2mtGCaMP6 probe (Fig. 3h). Plotting the mitochondrial versus cytosolic Ca^{2+} values revealed that MICU1 deficiency leads to the loss of the physiological cooperative sigmoid regulation of mitochondrial $[Ca^{2+}]$[7] (Fig. 3j), resulting in an elevated basal Ca^{2+} load in the organelle and in rapid response to changing cytosolic $[Ca^{2+}]$. These results were in accordance with the previously described function of the protein in other cell types[10]. In addition, the histamine-induced global peak $[Ca^{2+}]_c$ in the MICU1-deficient cells was significantly reduced (Fig. 3k,l). This finding is consistent with increased mitochondrial Ca^{2+} buffering, since the effect was prevented following the inhibition of mitochondrial Ca^{2+} uptake by the uncoupler FCCP (Fig. 3m) and ER Ca^{2+} content was unchanged in the MICU1 deficient cells (see Supplementary Fig. 12a).

Confocal imaging of mitochondria loaded with the potential-sensitive dye TMRM (Fig. 4a,b) or the Ca^{2+}-sensitive probe, rhod-2 (Fig. 4c,d) revealed that a significant proportion of the MICU1-deficient cells showed a highly fragmented mitochondrial network. In addition, the intensity of the rhod-2 fluorescence in those MICU1 mutant cells that showed a fragmented mitochondrial network was significantly increased, suggesting that mitochondrial fragmentation was associated with increased resting $[Ca^{2+}]_m$ (Fig. 4e). Moreover, re-expression of wild type MICU1 rescued this phenotype (Fig. 4f,g; Supplementary Figs.14 and 15). Together, these data show that loss of MICU1 leads to the chronic activation of the MCU channel even at resting $[Ca^{2+}]_c$, and hence to Ca^{2+}-induced fragmentation of the mitochondrial network.

As raised matrix $[Ca^{2+}]_m$ activates the tricarboxylic acid cycle[18] it has also been suggested that MICU1 regulates Ca^{2+}-mediated activation of mitochondrial energy metabolism through its role as the Ca^{2+} sensor of the MCU complex[10]. NAD(P)H autofluorescence was significantly increased in the MICU1 deficient cells, consistent with this model (Fig. 4h,i). Measurements of NAD(P)H fluorescence following histamine stimulation reveals the maximal $[Ca^{2+}]_m$ mediated change in energy metabolism[20]. This was not significantly different between the control and MICU1 deficient patient cells (Fig. 4i), consistent with the aequorin measurements of peak histamine stimulated $[Ca^{2+}]_m$ (see Fig 3a,c). The small but significant increase in NAD(P)H following histamine stimulation of MICU1 deficient patient cells (Fig. 4i) shows that the increase in resting $[Ca^{2+}]_m$ in these cells was not sufficient to saturate the Ca^{2+} dependent metabolic pathway. No significant differences could be detected in either basal or histamine-induced mitochondrial O_2 consumption, nor in

respiratory control or respiratory reserve capacity in control and MICU1-deficient fibroblasts, (Fig. 4j,k), in keeping with the unchanged $\Delta\Psi_m$ (see Fig. 3d).

These data show that loss of MICU1 results in a complex cellular phenotype due to increased mitochondrial Ca^{2+} load, already at basal cytoplasmic $[Ca^{2+}]$ or following spontaneous, low frequency cytoplasmic Ca^{2+} transients (see Supplementary Fig. 12b-e). The reduction in cytoplasmic Ca^{2+} signals as a result of enhanced mitochondrial Ca^{2+} buffering could disturb Ca^{2+}-dependent processes such as muscle contraction or synaptic transmission. Furthermore, the chronic activation of the MCU channel and subsequent chronic elevation of the mitochondrial matrix Ca^{2+} load may lead to moderate mitochondrial stress, as reflected by the fragmented phenotype seen in a proportion of cells. However, at least under resting conditions, the fibroblasts appear to compensate for the stress-induced dysfunction, without apparent defects in overall cellular metabolic function. The slow progression of the clinical features in affected patients appears to be consistent with limitations of these compensatory mechanisms *in vivo* in the long term.

The dysfunction of mitochondrial Ca^{2+} uptake described in these patients results in a novel phenotype, the clinical and pathological features of which overlap with those of muscular dystrophies, congenital core myopathies and mitochondrial myopathies. Mitochondrial damage and dysfunction are features common to these disorders. In Duchenne muscular dystrophy, sarcolemmal damage leads to dysregulation of cellular Ca^{2+} homeostasis, and mitochondrial Ca^{2+} overload-induced necrosis of myocytes[3]. In Ullrich congenital muscular dystrophy, the deficiency of collagen VI causes defects in mitochondrial architecture, Ca^{2+} dysregulation, and cell death[21]. In core myopathies, mutations in the type 1 ryanodine receptor (*RYR1*) gene lead to Ca^{2+} leak from the sarcoplasmic reticulum (SR) and consequent muscle dysfunction[4]. In these diseases, early pathological changes affect confined areas of muscle fibres. Within these, initial mitochondrial or SR disruption causes loss of local Ca^{2+} sequestration, causing mitochondrial swelling and disruption, and eventually complete loss of mitochondria from the cores[4].

The increased velocity of mitochondrial Ca^{2+} uptake and resting mitochondrial Ca^{2+} loading that we have seen in patients with MICU1-deficiency defines a new mechanism underlying neuromuscular disease; a primary defect in mitochondrial Ca^{2+} uptake. The phenotype described provides a much-needed *in vivo* insight into the biological role of this regulator of mitochondrial Ca^{2+} signalling.

URLs

http://sourceforge.net/projects/snpviewer/

http://www.LOVD.nl/MICU1

AUTHOR CONTRIBUTIONS:

ES, FM, MRD, and GS designed the study and experiments;

ES, FM, AMC, KP, DTB,MK, EHN, WLvdP, DL, and HR identified, consented and recruited the study subjects and provided clinical information;

DAP, CVL, CAJ, JEM, MK, IG, JTD, YS and MH, generated and analyzed clonal sequencing data;

CVL, GW, NR, KS, CAJ, SN, ZAA, and ST performed genetic analysis, confirmation studies and haplotyping;

JS, GS, DD, AR, RR and MRD performed calcium handling, cellular imaging, O_2 consumption and protein expression studies;

CAS, RP, IM, RAF undertook muscle immunohistochemistry and analysis on patient muscle biopsies;

ES, CVL, DTB, FM, GS and MRD wrote the manuscript.

FIGURE LEGENDS

Figure 1. Quadriceps biopsies from affected individuals. (**a**) Haematoxylin and eosin stained section from the biopsy of patient 4 at 7.3 years showing a mild excess of internal, and central nuclei in type I fibres. (**b**) A cluster of basophilic regenerating fibres with prominent vesicular nuclei in the biopsy from patient 3a at 3.3 years. These fibres label strongly for developmental myosin (**b**, inset), a marker of regeneration. (**c,d**). Sections stained for NADH-TR from the biopsies of patient 3a at 3.3 years (**c**) and patient no. 8b at 10.7 years(**d**) showing good fibre typing and areas devoid of stain in fibres of both intensity (minicore-like areas). Scale bar 50 μm.

Figure 2. Mutations in *MICU1* were identified in a multiplex consanguineous family. Pedigree of a consanguineous family with four affected children (**a**). A region of homozygosity shared between affected individuals V:1, V:4 and V:5 in the pedigree (**a**) is displayed using SNPviewer and is situated on chromosome 10 between 73.8 – 78.7 Mb (**b**). Variants identified from whole exome sequencing were confirmed by Sanger sequencing and annotated on the MICU1 transcript (**c**). qPCR showed significant loss of MICU1 messenger RNA in patients with both mutations. Bar chart shows mean values +/- SEM from three replicates. One-way ANOVA was used with *post-hoc* Bonferoni tests between each sample. *** < 0.001 (**d**).

Figure 3. Loss of MICU1 leads to increased mitochondrial Ca^{2+} load and reduced cytoplasmic Ca^{2+} transients without altering $\Delta\Psi_m$. Histamine induced mitochondrial (**a-j**) and cytoplasmic (**k-m**) Ca^{2+} signals were measured in primary fibroblasts from age matched healthy individuals (controls) and two patients carrying MICU1 mutations (ΔMICU1 8a and 6). For $[Ca^{2+}]_m$ measurements cells were transduced with an adenoviral mtAEQwt vector (**a-c**) and luminescence of cell populations were measured or cells were loaded with rhod-2 AM and mitochondrial regions of interest (ROI) were analysed by imaging (**e-j**) as described in the Online Methods (scale bar 10 μm). Basal $[Ca^{2+}]_m$ was further assessed by imaging 2mtGCaMP6 expressing cells (**h**). $[Ca^{2+}]_c$ was measured either in cytoplasmic ROIs in rhod-2 AM loaded cells or in a population of fluo-4 loaded cells using fluorimetry as described in Supplementary Methods. Cytoplasmic and mitochondrial rhod-2 intensity traces (**f,g**) were obtained from nuclear (where mitochondrial buffering of Ca^{2+} does not occur) and mitochondrial ROIs, respectively, as indicated in **e**. The rate of mitochondrial Ca^{2+} uptake (**b, i**) was quantified by calculating the time taken to reach half of the peak values (**c, f, g**). The aequorin and fluo-4 signals were calibrated into $[Ca^{2+}]$ values, as described in Supplementary Methods. Steady state intensity of TMRM was measured using confocal microscopy (**d**). a and c show representative traces, bar charts and f, g, j show mean ± SEM from >9 traces from 3 separate experiments. For pairwise comparisons of means (**i**) t-test, otherwise one-way ANOVA was used with *post-hoc* Bonferoni tests between each sample. * p < 0.05.

Figure 4. The effect of MICU1 loss on mitochondrial morphology, basal $[Ca^{2+}]_m$ and mitochondrial energy metabolism. Primary fibroblasts from age matched healthy individuals (controls) and two patients carrying MICU1 mutations (ΔMICU1 8a and 6) were loaded with fluo-4-AM to visualise cell boundaries (green) and either TMRM (**a, b**) or the Ca^{2+} sensitive dye rhod-2-AM (**c, d**), accumulating in mitochondria due to their positive charge (grey scale). Cells (>100/sample from at least 3 separate experiments) were scored according to the morphology of their mitochondrial network, and the percentage of cells with a fragmented network is shown (**a, c**). **b** and **d** middle panels show magnification of mitochondrial networks (scale bar 20 μm) . **e**, the intensity of rhod-2 was quantified in control and MICU1 mutant cells and grouped according to mitochondrial morphology, following background subtraction and thresholding of confocal images (see Supplementary Methods).

In **f, g** MICU1 was expressed in control and ΔMICU1 (8a and 6) cells using an adenoviral construct which also expressed GFP. TMRM (**f**) and rhod-2 (**g**) loaded cells were imaged using a high content imaging system (ImageXpress, see Supplementary Methods) and GFP positive and negative cells were analysed for morphology (**f**) or basal mitochondrial $[Ca^{2+}]$ (**g**). Details of the morphology scoring and normalisation of the rhod-2 signal is described in Supplementary Figs. 14 and 13, respectively, see also Supplementary Methods. In panel **h, i** NAD(P)H fluorescence was imaged using UV confocal microscopy in resting and histamine (10 μM) stimulated cells (scale bar 10 μm) . **j,** Oxygen consumption of intact control and MICU1 mutant fibroblasts was measured in suspension using high resolution respirometry (see Supplementary Methods). Basal, leak (in the presence of 2.5 μM oligomycin) and maximal respiration (in the presence of 1 μM FCCP) are shown. Panel **k** shows the effect of histamine (10 μM) on basal respiration, measured 1 min after the addition of the agonist. The number of images and cells analysed in **f**, **g** are described in the Supplementary Methods. For pairwise comparison of means t-test (**k**), otherwise one-way ANOVA was used with *post-hoc* Bonferoni tests between each sample Bar charts show mean ± SEM values from 3 separate experiments. * $p < 0.05$.

ONLINE METHODS

Research subjects

All families provided written informed consent, and this study was approved by the boards of the Leeds East and Great Ormond Street Hospital Research Ethics Committees (Refs Leeds East 07/H1306/113 and GOSH 00/5802 respectively) and the institutional review board of the University of Leiden. Patients were recruited from the muscle clinics of the above institutions. We used standard methods to isolate genomic DNA from peripheral blood of the affected children and family members or from frozen fetal tissue or amniocytes. Chromosome analysis was performed for at least one affected individual of each family.

Histology, histochemistry and immunohistochemistry

All histological and histochemical studies, H&E, NADH, SDH and COX, were performed on frozen sections (10 μm)[22]. Immunohistochemical studies were performed at the room temperature. Briefly, unfixed frozen serial sections (7 μm) were incubated with primary antibodies (foetal/neonatal myosin, mouse monoclonal WB-MHCn (Abcam, ab49461), 1:15, and embryonic myosin, mouse monoclonal Rnmy/9D2 , 1:20, (Leica,Novacastra, NCL-MHCd) for 1 hour followed by three washes in phosphate buffered saline (PBS) at pH 7.2. The sections were then incubated with the appropriate biotinylated secondary antibodies (GE Healthcare Life Sciences, RPN1001) for 30 minutes followed by streptavidin peroxidase HRP 1:150 for 30 minutes. After washes, the sections were developed with 3,3-diaminobenzidine for 10 minutes.

SNP genotyping and data / variant annotation.

Birdseed genotype files generated by the Affymetrix Genotyping Console[TM] were analysed using SnpViewer (see URLs) to identify concordant regions of homozygosity. A single homozygous region shared between affected individuals was found between

RS1668169;RS10824473 on chr10:73,825,652-78,713,115 containing 42 RefSeq genes; 457 non-redundant RefSeq coding exons (76.4 kb).

Whole exome sequencing

Alignment and variant calling:

Target capture was performed using the Agilent SureSelect All Exon v4 exome enrichment kit according to standard manufacturer protocols. Sequencing of 80 bp reads was performed using an Illumina GAIIx. Reads were aligned to GRCh37 using novoalign (Novocraft Technologies, Selangor, Malaysia) and processed using the Genome Analysis Toolkit (GATK)[23] and Picard (see URLs) to perform indel realignment and duplicate removal. SNV and indel variants were called using the UnifiedGenotyper feature of the GATK.

Filtering:

Bespoke perl scripts were used to remove variants present in dbSNP129 or with a minor allele frequency ≥ 1 % in dbSNP132 and to annotate functional consequences. Variants present in another 22 in-house exomes were also removed. Of the RefSeq coding bases within the autozygous region identified in family 1, 91.9 % were covered by at least 5 good quality reads (minimum phred-like base quality 17 and minimum mapping quality of 20).

We selected for variants causing indels within coding regions, non-synonymous SNVs or alteration of splice consensus sequences. Following the filtering described above, three such variants were identified in the autozygous region identified in family 1, comprising two missense SNVs in DUSP13 (NM_001007273: c.223A>G,p.S75G and c.746G>A,p.C249Y) and alteration of the invariant splice acceptor site in *MICU1*. Both missenses were predicted benign by Polyphen, SIFT and Condel and had a global MAF greater than 30 % in 1000 genomes data leaving the splice site mutation in *MICU1* as the only likely pathogenic variant (NM_001195518: c.1078-1G>C).

Mutation analysis

Primers were designed for all coding exons of *MICU1* using Primer3 (supplementary table 2)[24]. Direct sequencing was performed using the dideoxy chain termination method (ABI "BigDye 3.0" system) on an ABI 3730 DNA sequencer, and sequences analyzed using 4Peaks software.

Gene expression analyses with quantitative real-time PCR.

MICU1 expression in patient and control fibroblasts was analysed with quantitative real-time PCR. Total RNA was converted to cDNA using the Superscript III first-strand cDNA system (Life Technologies). PCR analysis of cDNA was performed using PAGE-purified primers specific for human *MICU1*(Sigma-Aldrich), after optimization to eliminate primer-dimers and subsequent confirmation by analysis of amplimer dissociation curves after a quantitative PCR run. Each reaction was run in triplicate. Amplimer levels were quantified continuously

with the SYBR GreenER qPCR system (Invitrogen) using an ABI 7500 instrument, essentially as described previously[25]. 36B4 cDNA was amplified for normalization.

Cell culture

Skin biopsies were taken from patients after obtaining informed patient consent. Control skin samples were obtained from paediatric patients (undergoing surgical procedures) with no known neuromuscular disease following written informed research consent. Fibroblasts were grown from skin explants and cultured in Dulbecco's modified Eagles medium (Invitrogen) supplemented with 20% foetal bovine serum (Invitrogen), 1% L-glutamine (Sigma) and 1% penicillin, streptomycin and neomycin (Sigma) at 37 °C in 5% CO_2. Patient cell-lines were confirmed to be harbouring the correct, homozygous mutation in *MICU1* by Sanger sequencing prior to functional studies. Cell lines were routinely tested for mycoplasma contamination.

MICU1 expression and western blotting

The adenovirus expressing MICU1-HA and GFP were created using the AdEasy strategy (Stratagene). Adenoviral vectors contain two distinct promoters that independently drive the expression of the gene of interest and of GFP. Therefore mock plasmid expresses only GFP protein. Cells were grown in Dulbecco's modified Eagle's medium (DMEM) (Invitrogen), supplemented with 10% fetal bovine serum (FBS) (Invitrogen) and infected with the different adenoviruses at a MOI (multiplicity of infection) of 50 pfu/cell.

After 48 hours of expression cells were lysed in RIPA lysis buffer (1% Triton X-100, 0.1% SDS, 50 mM Tris-HCl pH 7.4, 150 mM NaCl, 0.5% Sodium Deoxycholate, 1 mM EDTA and Complete EDTA-free protease inhibitor mixture (Roche Applied Science) and quantified with the BCA method (Pierce). 40 µg of total proteins were separated by SDS-PAGE gel electrophoresis, transferred to Hybond-C Extra membrane (Amersham) and stained with Ponceau S solution. MICU1-HA was visualised with a polyclonal α-HA antibody (Sigma). All the antibodies were used at a dilution of 1:1000 and were from Sigma (MCU - hpa016480; MICU1 - hpa037480) or Santa Cruz (-TOM20). Secondary, HRP-conjugated antibodies (1:5000) were from BioRad (170-6515 and 170-6516).

Immunofluorescence and analysis of ER-mitochondrial co-localisation

Control and MICU1 mutant cells were plated on glass coverslips and either left untreated or were treated with 1 µM thapsigargin for 24h. Cells were fixed in 4% paraformaldehyde (20 min, RT), washed in PBS (5min) and blocked in PBS containing 1% BSA and 1% FBS (1h, RT). Primary antibodies (grp75, sc-1058, Santa Cruz; PDI-A3, hpa003230, Sigma) were used at 1:200 dilution (O/N 4ºC). For visualisation of grp-75 (mitochondria) and PDIA3 (ER) the appropriate Alexa488 and 594 conjugated secondary antibodies were used, respectively (1h, RT, 1:200, Invitrogen). Cells were imaged using a Zeiss 700 CLSM confocal system, with 488 and 535nm lasers for excitation, emission settings for optimal separation, calculated by the Zeiss ZEN acquisition software, and 63x/1.4NA/oil objective. Z-series of images were acquired using <1AU pinhole diameter and <400nm distance between Z-

planes. Settings for the acquisition and thresholding were kept standard for the whole experimental set. Co-localisation of the red and green signals was quantified the JACoP v2.0 plugin (http://rsbweb.nih.gov/ij/plugins/track/jacop.html)[26] in ImageJ. Mander's coefficients of the two signals to estimate of the amount of co-localizing signal from a channel over another were calculated and shown. To visualise co-localizing pixels the resulting Costes overlay images were used.

Live cell confocal imaging of mitochondrial membrane potential and NAD(P)H

Confocal imaging was used to measure mitochondrial membrane potential, mitochondrial resting Ca^{2+} content, NAD(P)H redox state and to assay mitochondrial morphology. For all imaging experiments cells were grown on 22mm glass coverslips or 35mm imaging dishes (WPI). Measurements were carried out in recording buffer (RB [in mM]: NaCl 138, KCl 5.6, $NaHCO_3$ 4.2, NaH_2PO_4 1.2, $MgCl_2$ 1.2, $CaCl_2$ 2.6, D-glucose 10, HEPES 10). All images were acquired on a Zeiss 700 CLSM or a Zeiss 510 UV-VIS CLSM. For measurements of mitochondrial membrane potential cells were equilibrated with tetramethyl rhodamine methyl ester (TMRM, 25nM, 30 min, 37ºC) before placing on the heated stage of the CLSM and images were acquired using a 63x/1.4 NA/oil objective. The dye was present throughout imaging. Fluorescence was excited at 535nm and measured at >560nm. Z stacks were acquired and maximal projections were used for quantification to avoid a bias in the focal plane. NAD(P)H imaging was carried out using the Zeiss 510 UV-VIS CLSM with the pinhole wide open to maximise signal. Fluorescence was excited using the 351nm line of an Argon laser and measured between 435 and 485 nm. ImageJ or the Zeiss Zen analysis software were used for image analysis. Images were thresholded to quantify the mean of mitochondrial localised signal intensities. Identical acquisition settings and threshold values were used throughout the set of experiments.

Mitochondrial and cytosolic Ca^{2+} measurements

Mitochondrial [Ca^{2+}] measurements with aequorin

Dynamic mitochondrial [Ca^{2+}] measurements were performed in cells transduced with the mitochondrial targeted luminescent aequorin probe mtAEQ, encoded by an adenoviral construct as previously described[1]. Cells were seeded in 96 well plates (50,000/well) and histamine (10 µM) induced mitochondrial signals were measured in a luminescence plate reader (Fluostar Optima, BMG Labtech, UK) using 3mm luminescence optics and light guide after 48h of viral transduction. Prior to measurements cells were reconstituted with coelenterazine (Invitrogen) for 2h at 37ºC and luminescence values converted into [Ca^{2+}] as previously described (Traba et al. PMID 22015608).

Mitochondrial [Ca^{2+}] measurements with rhod-2

Measurements of resting mitochondrial [Ca^{2+}] were made using cells loaded with 5µM rhod-2 AM for 30 min at R.T. prior to washing and confocal imaging (ex=535nm em>560nm, Zeiss 700 CLSM). Images were background corrected by subtracting mean pixel values of a cell-

free ROI. Dynamic mitochondrial [Ca^{2+}] measurements were carried out on cells loaded with 5μM rhod-2 AM for 20 min at R.T., followed by 10 min incubation at 37ºC. For imaging an Olympus IX71 inverted epifluorescence microscope (Olympus) fitted with a computer controlled motorised stage (Applied Scientific Instrumentation) with a 40x fluorite objective lens (N.A. 0.6/air) and a full-enclosure environmental chamber heated to 37°C (Digital Pixel Imaging, Brighton, UK). Images were collected using a Hamamatsu C10600-10B CCD camera (Hamamatsu Corporation), and recorded using MetaFluor 7.8 (Universal Imaging). Illumination was provided by light from a metal halide arc lamp passing through a computer controlled filter wheel (Prior Scientific) and a 84000v2 Quad filter set (Chroma Technology), using a D-350/50x excitation filter. To achieve high temporal resolution 50ms acquisition time were used and streamed into the computers RAM, and images were saved following a run of approximately 1 min. Images were analysed using MetaFluor Analyst. Nuclear (representing cytosolic values without mitochondrial buffering) and mitochondrial regions were measured from each cell, following background correction by subtracting mean pixel values of a cell-free ROI in each frame. Fluorescence intensity values were normalised to the initial cytosolic values.

Mitochondrial [Ca^{2+}] measurements with 2mtGCaMP6m

In order to test resting [Ca^{2+}]$_m$ with high sensitivity, we developed a new calcium probe based on the last generation GCaMP probe[27] targeted to the mitochondrial matrix. We chose the GCaMP6m version, due to its highest calcium affinity, with its K$_d$ (167 nM) in the range of normal resting [Ca^{2+}]$_m$. 2mtGCaMP6m was obtained by the addition of 2 tandem mitochondrial targeting sequences (derived from COX8A of human origin) to the GCaMP6m sequence (Addgene plasmid 40754) and was created by custom gene synthesis (Life Technologies). In order to be independent of basal fluorescent intensity variations due to the variable expression levels of the probe, we took advantage of the isosbestic point in GCaMP6m excitation spectrum: we experimentally determined in living cells that exciting GCaMP6m at 410 nm leads to fluorescence emission which is not Ca^{2+}-dependent. As a consequence, the ratio between 474 and 410 nm excitation wavelengths is proportional to [Ca^{2+}] while independent on probe expression levels. Fibroblasts were grown on 24 mm coverslip and transfected with 2mtGCaMP6m encoding plasmid using Lipofectamine LTX according to manufacturer's instruction (Life Technologies). After 36 hours, coverslips were placed in 1 mL of KRB buffer and imaging was performed on a Zeiss Axiovert 200 microscope equipped with a 63x/1.4 N.A. PlanApochromat objective. Excitation was performed with a Deltaram V high speed monochromator (Photon Technology International) equipped with a 75W Xenon Arc lamp. Images were captured with a high sensitivity Evolve 512 Delta EMCCD (Photometrics). The system is controlled by Metamorph 7.5 and was assembled by Crisel Instruments. Cells were thus alternatively illuminated at 474 and 410 nm and fluorescence was collected through a 515/30 nm bandpass filter (Semrock). Exposure time was set to 300 ms. At least 5 fields were collected per coverslip, and each field was acquire for 20 s (0.5 frame/s). Analysis were performed with the Fiji distribution of ImageJ[28]. Both images were background corrected frame by frame by subtracting mean pixel values of a cell-free ROI. Data are presented as the mean ± S.E.M. of the averaged ratio of all time points.

Cytosolic [Ca^{2+}] measurements with fluo-4

Dynamic cytoplasmic [Ca^{2+}] measurements were performed in the same plate reader (Fluostar Optima, BMG Labtech, UK, see aequorin measurements) using fluorescence optics and light guide with 485BP12 excitation and Em520 emission filters in fluo-4-AM loaded (30 min R.T.) cells. To avoid leakage of the dye, RB was supplemented with 1 mM probenecid (Sigma). Calibration of the background (measured in an empty well with RB) corrected fluorescence intensities into [Ca^{2+}] was done using the following equation[29]:

$$[Ca^{2+}] = K_d \times (F/F_{max} - 1/R_f)/(1 - F/F_{max})$$
where K_d = 350nM, F_{max} = maximum fluorescence after ionomycin application, Rf = 100

High content imaging of mitochondrial morphology and basal mitochondrial [Ca^{2+}]

Control and ΔMICU (8a and 6) cells expressing MICU1 and GFP were imaged using

the ImageXpress Micro XL high content imaging system (Molecular Devices). Cells were seeded in 96 well thin bottom plates (BD Biosciences) and loaded in RB with either TMRM (25 nM, present during the whole experiments) or rhod-2 AM (5 μM, 20 min RT, followed by 30 min incubation in dye-free RB) and 1 μg/mL Hoechst 33342 (present during the experiment) to label nuclei for cell counting. Cells were imaged using a custom protocol to image 3 wavelengths (Lumencor solid sate illumination with Semrock [Brightline] filters (nm) ex377/50 em447/60 for Hoechst 33342; ex472/30 em520/35 nm for GFP ex531/40 em593/40 for TMRM and rhod-2), nine fields/well with a Nikon 40X Plan Apo NA 0.95 dry objective, binning 1 with a CMOS detector. Acquisition and analysis were performed using MetaXpress software. The workflow of quantification and morphology scoring are described in Supplementary Figure S11 and S12, respectively.

Oxygen consumption measurements

Cells were trypsinised and resuspended in HEPES (20 mM) buffered DMEM supplemented with 5.5 mM glucose, 2 mM glutamine and 1 mM pyruvate at 1 million cells/ml. Respiration rates were measured at 37ºC with the High Resolution Oxygraph (Oroboros Oxygraph-2k, Graz, Austria). Maximal oxidative capacities were determined in the presence of carbonyl cyanide 4-(trifluoromethoxy)phenylhydrazone (FCCP, 1 μM), state 4 respiration values were obtained in the presence of oligomycin (2.5 μM), non-mitochondrial (background) oxygen consumption was determined in the presence of Antimycin-A (2.5 μM).

Statistics

Sample sizes for functional measurements (listed in the legends of Figs. 3 and 4) were determined to achieve a statistical power of 0.95 using the G*Power 3.1.3 for Mac[30], depending on the required effect size which was considered biologically considerable. Where standard deviations exceeded the estimated value, sample sizes were increased. These calculations assumed normal distribution of the samples, two sided one-way ANOVA

or t-test to compare difference between means of two independent groups. Mean ± SEM values are shown on all figures. F-tests showed equal variance for all tests.
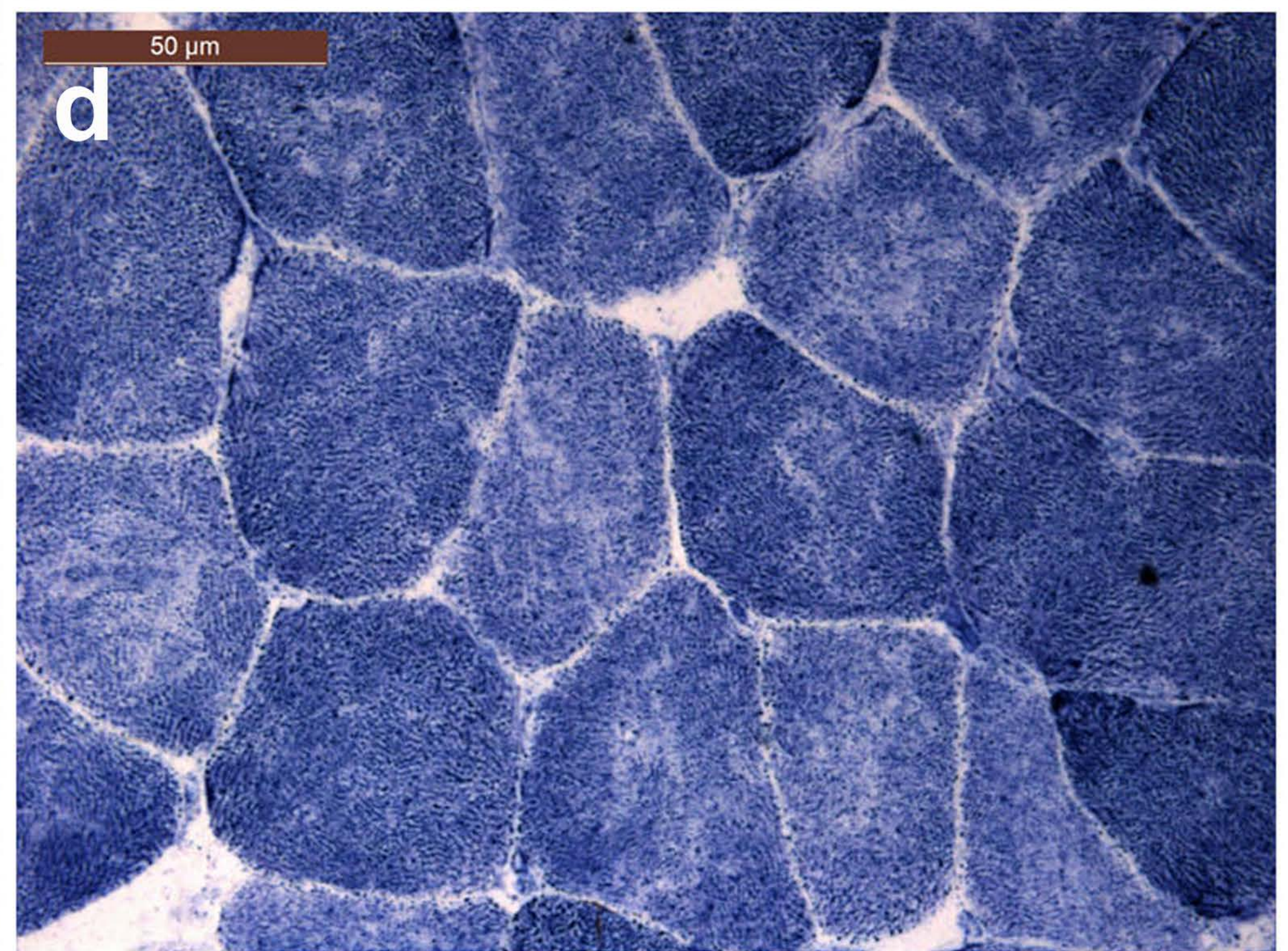
URLs

SnpViewer: http://sourceforge.net/projects/snpviewer/

Picard tools: http://picard.sourceforge.net/

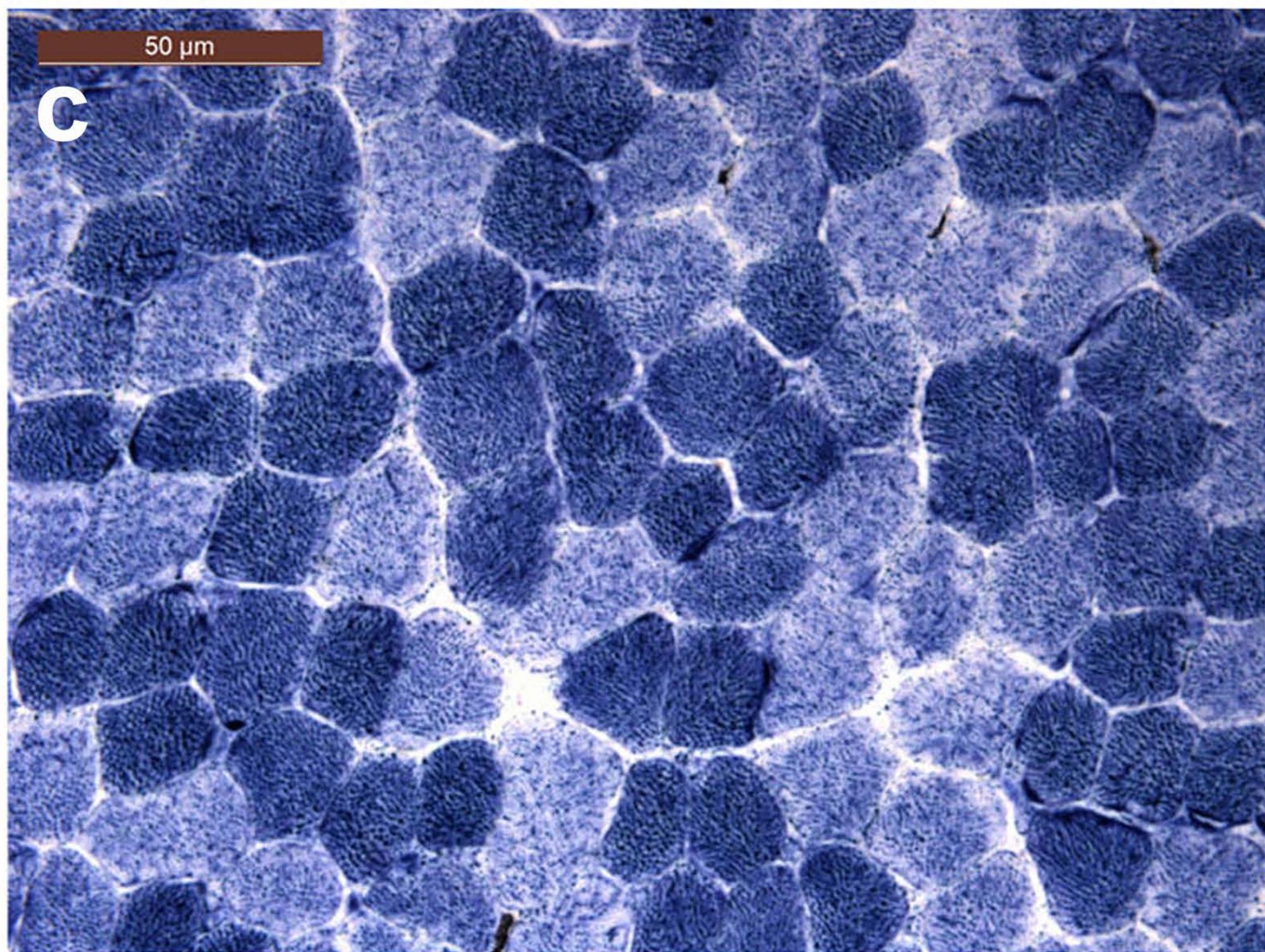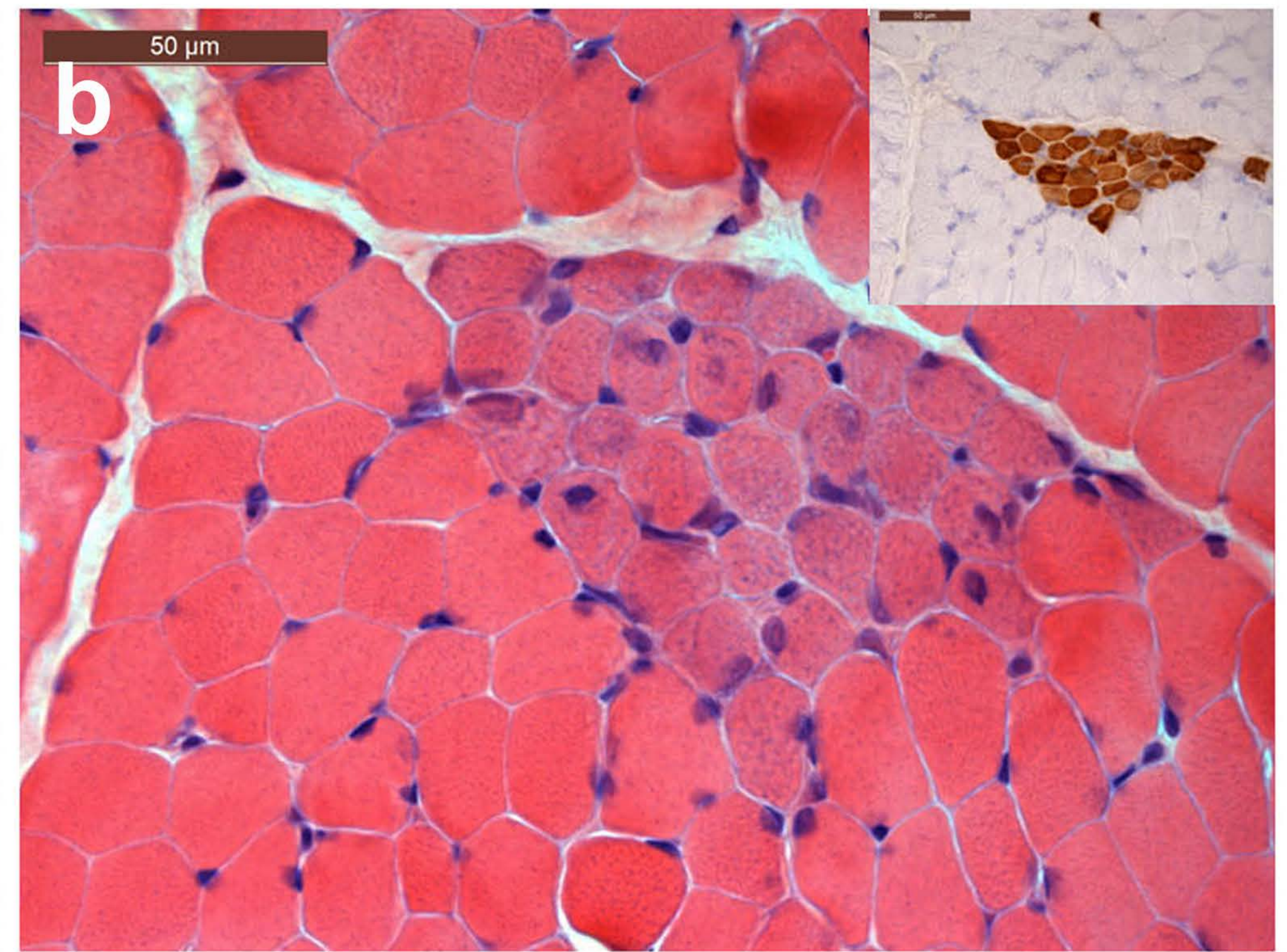Image J: http://rsbweb.nih.gov/ij/

Primer 3: http://bioinfo.ut.ee/primer3-0.4.0/
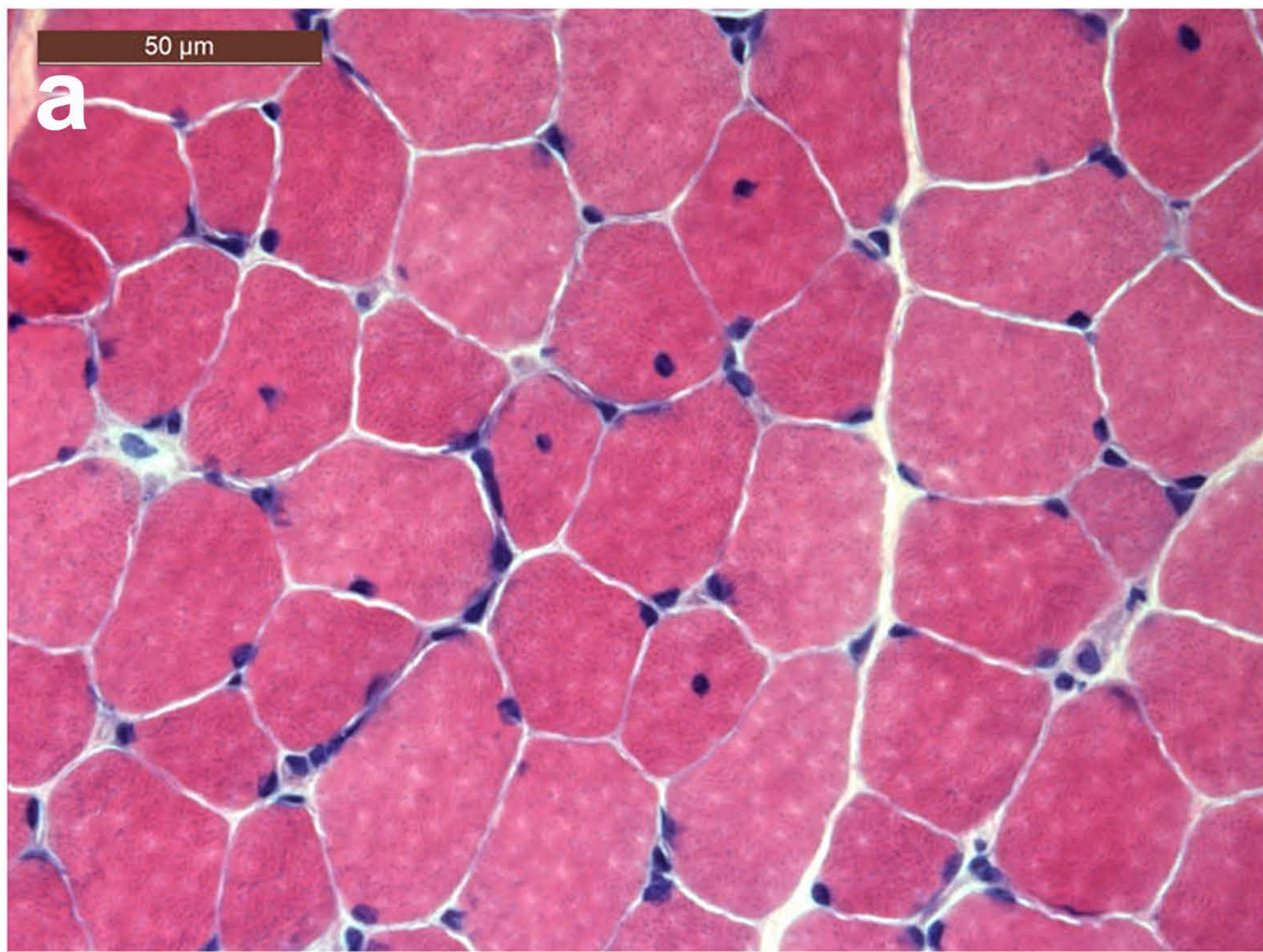
References

1   De Stefani, D., Raffaello, A., Teardo, E., Szabo, I. & Rizzuto, R. A forty-kilodalton protein of the inner membrane is the mitochondrial calcium uniporter. *Nature* **476**, 336-340 (2011).
2   Perocchi, F. *et al.* MICU1 encodes a mitochondrial EF hand protein required for Ca(2+) uptake. *Nature* **467**, 291-296 (2010).
3   Millay, D. P. *et al.* Genetic and pharmacologic inhibition of mitochondrial-dependent necrosis attenuates muscular dystrophy. *Nat Med* **14**, 442-447 (2008).
4   Boncompagni, S. *et al.* Characterization and temporal development of cores in a mouse model of malignant hyperthermia. *Proc Natl Acad Sci U S A* **106**, 21996-22001 (2009).
5   Duchen, M. R. & Szabadkai, G. Roles of mitochondria in human disease. *Essays Biochem* **47**, 115-137 (2010).
6   McCormack, J. G., Halestrap, A. P. & Denton, R. M. Role of calcium ions in regulation of mammalian intramitochondrial metabolism. *Physiol Rev* **70**, 391-425 (1990).
7   Szabadkai, G. & Duchen, M. R. Mitochondria: the hub of cellular Ca2+ signaling. *Physiology (Bethesda)* **23**, 84-94 (2008).
8   Rizzuto, R. & Pozzan, T. Microdomains of intracellular Ca2+: molecular determinants and functional consequences. *Physiol Rev* **86**, 369-408 (2006).
9   Giacomello, M., Drago, I., Pizzo, P. & Pozzan, T. Mitochondrial Ca2+ as a key regulator of cell life and death. *Cell Death Differ* **14**, 1267-1274 (2007).
10   Csordas, G. *et al.* MICU1 Controls Both the Threshold and Cooperative Activation of the Mitochondrial Ca(2+) Uniporter. *Cell Metab* **17**, 976-987 (2013).
11   Plovanich, M. *et al.* MICU2, a paralog of MICU1, resides within the mitochondrial uniporter complex to regulate calcium handling. *PLoS One* **8**, e55785 (2013).
12   Mallilankaraman, K. *et al.* MICU1 is an essential gatekeeper for MCU-mediated mitochondrial Ca(2+) uptake that regulates cell survival. *Cell* **151**, 630-644 (2012).
13   Baughman, J. M. *et al.* Integrative genomics identifies MCU as an essential component of the mitochondrial calcium uniporter. *Nature* **476**, 341-345 (2011).

14   Carr, I. M., Sheridan, E., Hayward, B. E., Markham, A. F. & Bonthron, D. T. IBDfinder and SNPsetter: tools for pedigree-independent identification of autozygous regions in individuals with recessive inherited disease. *Hum Mutat* **30** (2009).

15   Stevens, E. *et al.* Mutations in B3GALNT2 cause congenital muscular dystrophy and hypoglycosylation of alpha-dystroglycan. *Am J Hum Genet* **92**, 354-365 (2013).

16   Zampese, E. *et al.* Presenilin 2 modulates endoplasmic reticulum (ER)-mitochondria interactions and Ca2+ cross-talk. *Proc Natl Acad Sci U S A* **108**, (2011).

17   Chami, M. *et al.* Role of SERCA1 truncated isoform in the proapoptotic calcium transfer from ER to mitochondria during ER stress. *Molecular cell* **32**, 641-651 (2008).

18   Bianchi, K., Rimessi, A., Prandini, A., Szabadkai, G. & Rizzuto, R. Calcium and mitochondria: mechanisms and functions of a troubled relationship. *Biochim Biophys Acta* **1742**, 119-131 (2004).

19   Gerencser, A. A. & Adam-Vizi, V. Selective, high-resolution fluorescence imaging of mitochondrial Ca2+ concentration. *Cell calcium* **30**, 311-321 (2001).

20   Spat, A. & Pitter, J. G. The effect of cytoplasmic Ca2+ signal on the redox state of mitochondrial pyridine nucleotides. *Molecular and cellular endocrinology* **215**, 115-118 (2004).

21   Irwin, W. A. *et al.* Mitochondrial dysfunction and apoptosis in myopathic mice with collagen VI deficiency. *Nat Genet* **35**, 367-371 (2003).

22   Dubowitz, V., Sewry, C. A. & Oldfors, A. *Muscle biopsy : a practical approach*. 4th edn, (Saunders, 2013).

23   McKenna, A. *et al.* The Genome Analysis Toolkit: a MapReduce framework for analyzing next-generation DNA sequencing data. *Genome research* **20**, 1297-1303 (2010).

24   Rozen, S. & Skaletsky, H. Primer3 on the WWW for general users and for biologist programmers. *Methods Mol Biol* **132**, 365-386 (2000).

25   Dawe, H. R. *et al.* The Meckel-Gruber Syndrome proteins MKS1 and meckelin interact and are required for primary cilium formation. *Hum Mol Genet* **16**, 173-186 (2007).

26   Bolte, S. & Cordelieres, F. P. A guided tour into subcellular colocalization analysis in light microscopy. *Journal of microscopy* **224**, 213-232 (2006).

27   Chen, T. W. *et al.* Ultrasensitive fluorescent proteins for imaging neuronal activity. *Nature* **499** (2013).

28   Schindelin, J. *et al.* Fiji: an open-source platform for biological-image analysis. *Nature methods* **9** (2012).

29   Maravall, M., Mainen, Z. F., Sabatini, B. L. & Svoboda, K. Estimating intracellular calcium concentrations and buffering without wavelength ratioing. *Biophysical journal* **78**, 2655-2667 (2000).

30   Faul, F., Erdfelder, E., Buchner, A. & Lang, A. G. Statistical power analyses using G*Power 3.1: tests for correlation and regression analyses. *Behavior research methods* **41**, 1149-1160 (2009).
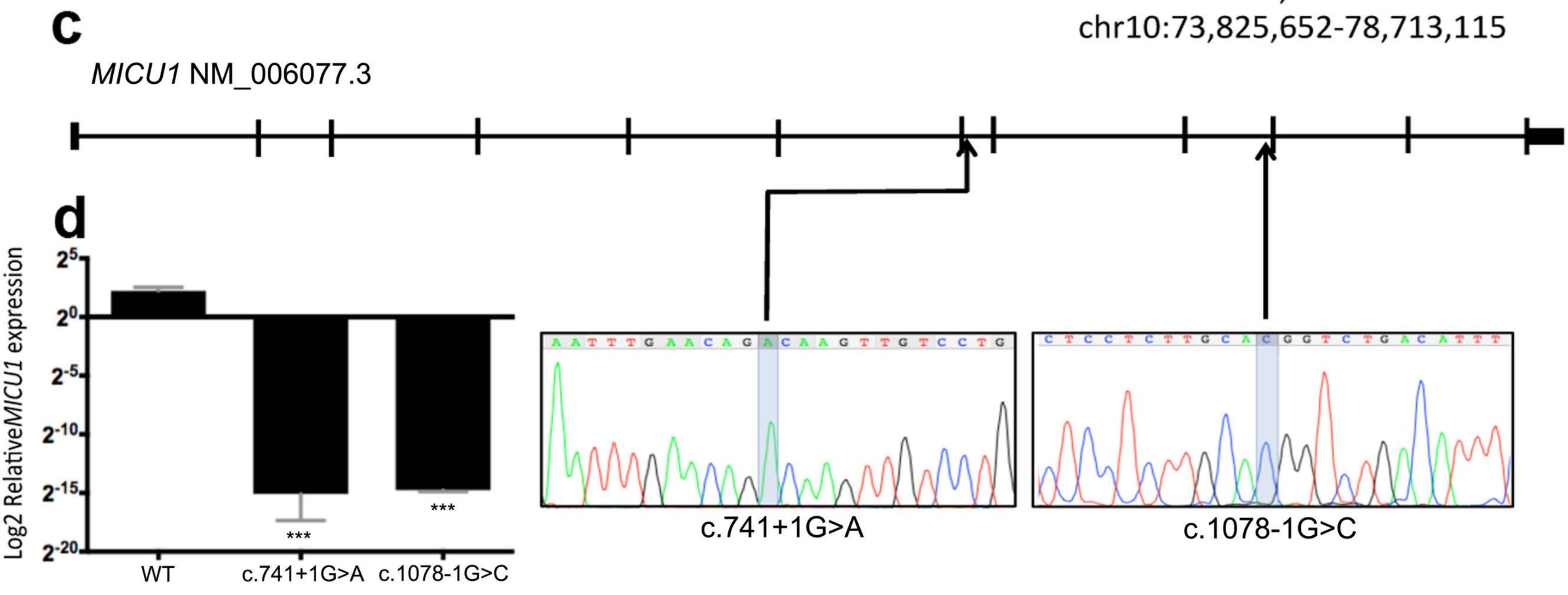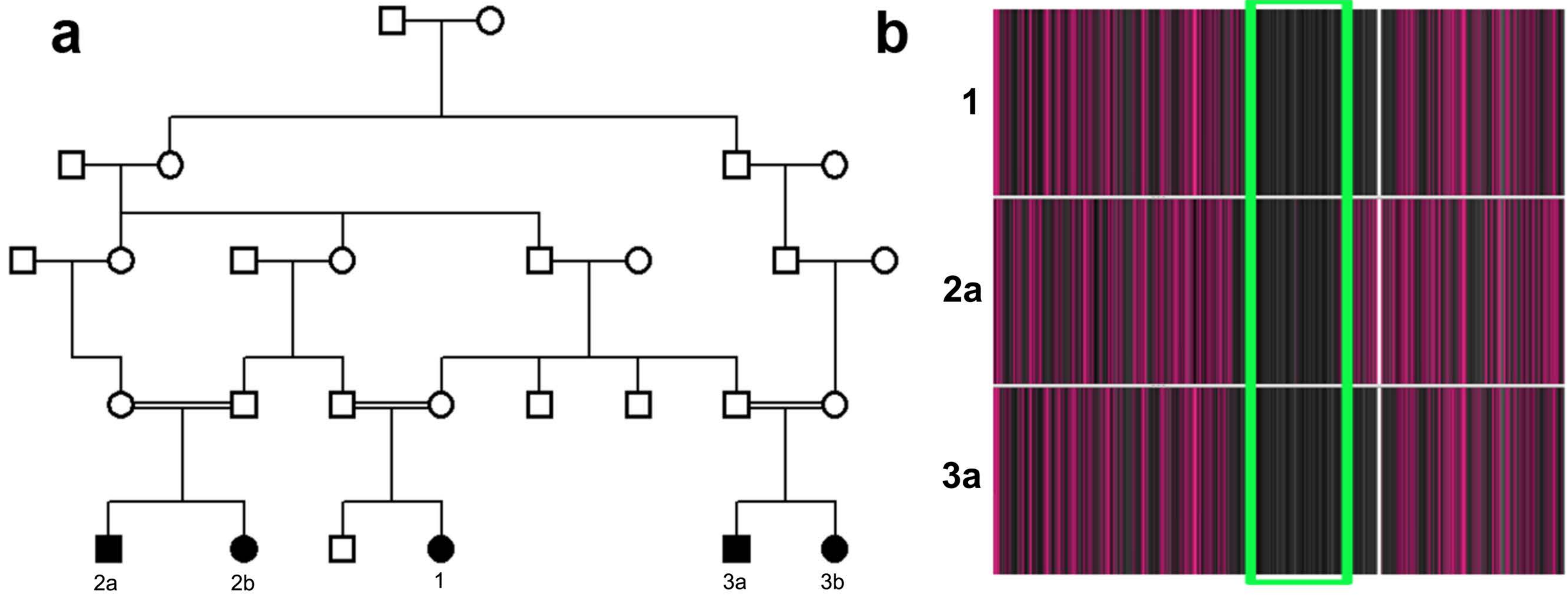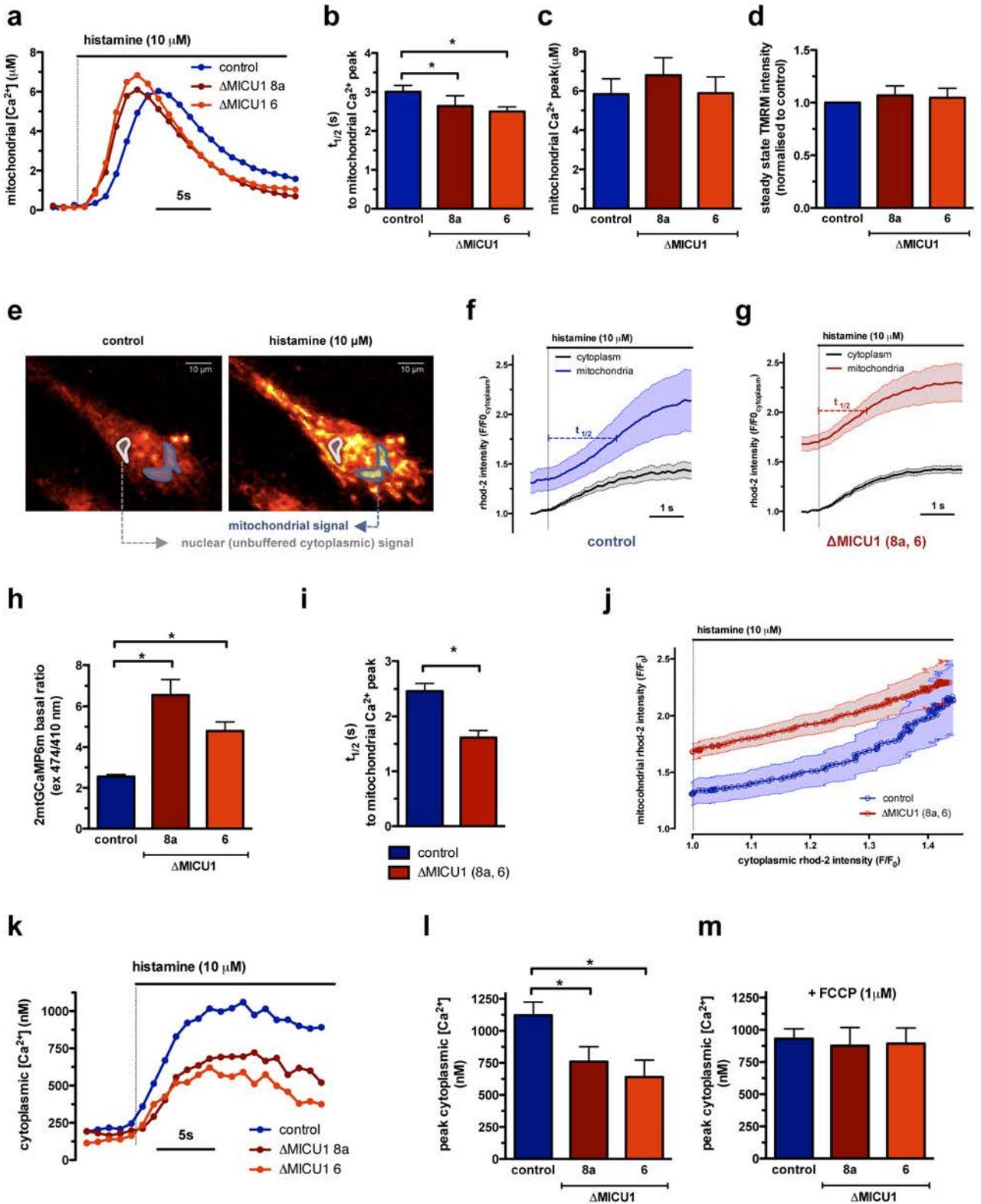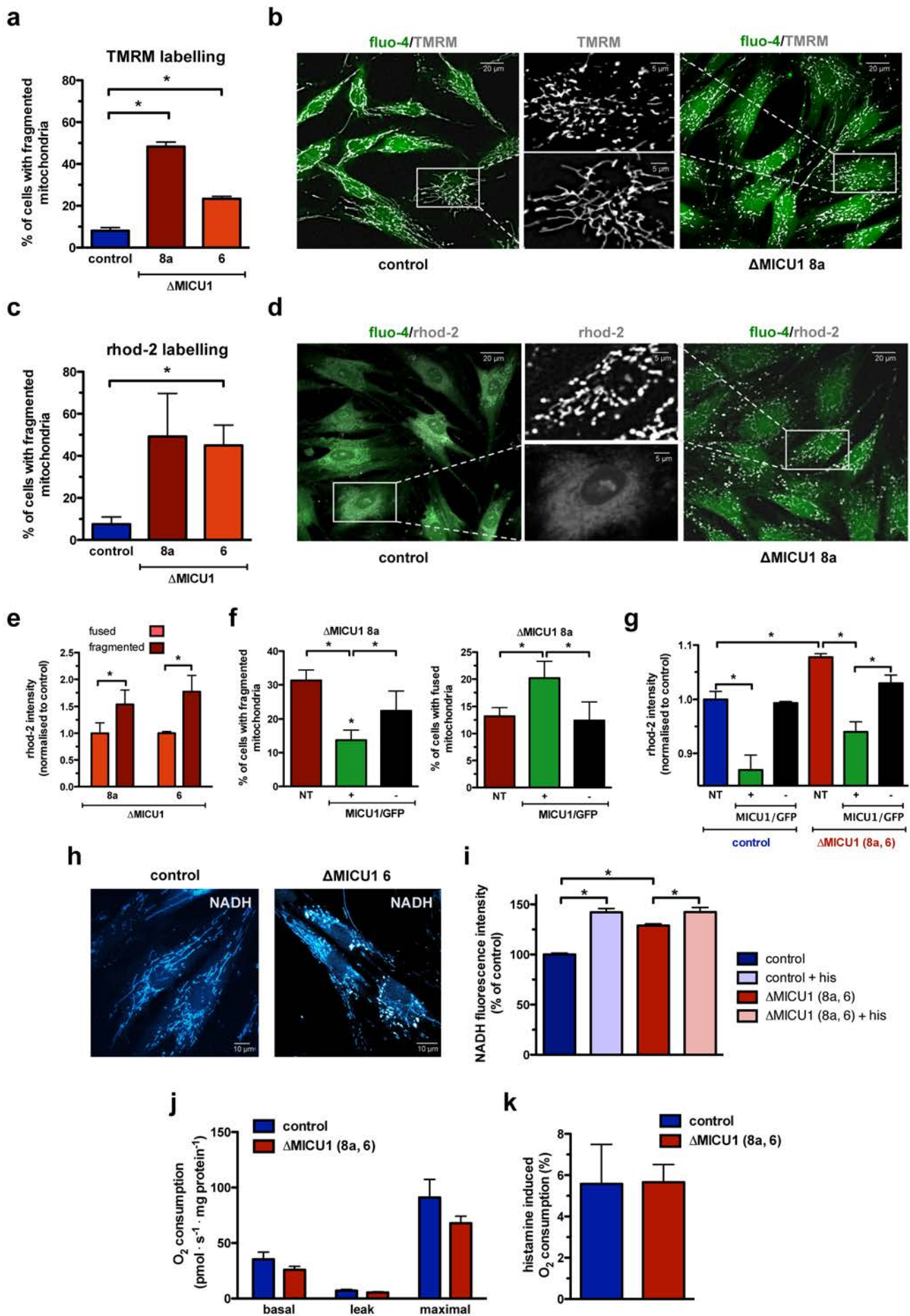
Figure 1

RS1668169;RS10824473
chr10:73,825,652-78,713,115

MICU1 NM_006077.3

c.741+1G>A

c.1078-1G>C

Figure 2

Figure 3

Figure 4